Energy Technology
Generation, Conversion, Storage, Distribution
www.entechnol.de

Design Optimization of Energy-Storing Hybrid Supercapacitor Composite for Electric Vehicle's Body Panel

*Deepak Pandey, Rajkumar Gurjar, Kowsik Sambath Kumar, Leaford Nathan Henderson, Maydenee Maydur Tresa, Luke Roberson, AbdulJabbar Mohammed Hussain, Nilesh Dale, and Jayan Thomas**

As electric vehicles (EVs) are evolving, innovative technologies like "energized composite" that can store energy in the car's body helps extend its range per charge. The composite's unique ability to function as both structural body panel and charge storage medium stems from its unique pattern design between "electrochemical areas (EcA)" and "epoxy area (EpA)". Herein, a design optimization study is presented to obtain a balanced ratio between EcA versus EpA to maximize the charge storage ability of the composite while maintaining a decent tensile and bending strength. Simulations using ANSYS software and experimental confirmation using universal testing machines and electrochemical analyzers are used to derive optimum ratios between EcA and EpA. Uniaxial tension test and 3-point bend test have been performed to optimize the tensile and bend strengths, whereas cyclic voltammetry, galvanic charge–discharge, and electrochemical impedance spectroscopy are used to determine the electrochemical performance of various design configurations by modulating the ratios of EcA versus EpA. Overall, the highest achieved energy storage per lamina is 2531 mWh m^{-2} for a maximum of 81.6% EcA with a tensile strength of 417.73 MPa and bending strength of 263.13 MPa. This study is highly beneficial for EVs and aerospace applications.

1. Introduction

With the rising concerns over global warming, there is a serious effort to utilize renewable energy sources and store the energy harvested in highly efficient energy storage systems.[1,2] Globally, there are many initiatives to reduce carbon emissions through various means; one of them is the mass adoption of electric vehicles (EVs). Though EVs are becoming increasingly popular, most of the general population still expresses range anxiety as one of the major reasons for their nonadoption.[3] As the automobile manufacturers are focusing on increasing the range of their new EV models by adding more batteries to the existing pack, the overall weight of the vehicle increases, which mitigates the increase in range to a certain extent, causing looping challenges for the EV range.

We recently developed a dual-function carbon fiber-based composite to address these multiple engineering challenges in extending the range of EVs. These composites are not only lightweight and super strong but can store electrical charge (to supplement the existing EV battery pack) and be molded to any shape.[4] We have termed this composite as "energized composite" or e-CFRP (energized carbon fiber reinforced polymer) composite. We proposed its use as the body shell (body panels) of future EVs.[4] Energized composites are made from carbon fiber electrodes, where graphene sheets are vertically attached to carbon fibers to enhance the surface area.[5] Then metal oxides like Mn_3O_4 and MoO_2 are used as cathode and anode coating on graphene to provide high work function difference, which helps in increasing the voltage.[6] Further, these anodes and cathodes are assembled using a patterned approach between electrolyte and epoxy and are cured at a

D. Pandey, R. Gurjar, K. S. Kumar, L. N. Henderson, M. M. Tresa, J. Thomas
Department of Materials Science and Engineering
University of Central Florida
Orlando, FL 32816, USA
E-mail: Jayan.Thomas@ucf.edu

D. Pandey, R. Gurjar, K. S. Kumar, L. N. Henderson, M. M. Tresa, J. Thomas
NanoScience Technology Center
University of Central Florida
Orlando, FL 32826, USA

The ORCID identification number(s) for the author(s) of this article can be found under https://doi.org/10.1002/ente.202200726.

DOI: 10.1002/ente.202200726

L. Roberson
NASA Kennedy Space Center
Merritt Island, FL 32899, USA

A. J. Mohammed Hussain, N. Dale
Advanced Materials & Technology Research
Nissan Technical Center North America
Farmington Hills, MI 48331, USA

J. Thomas
CREOL
College of Optics and Photonics
University of Central Florida
Orlando, FL 32816, USA

certain temperature and pressure to develop a high-strength, energy-storing carbon fiber composite.[4,7] The energy stored in the body shell supplements the existing battery energy storage. When it comes to the safety concerns regarding storing energy in the body shell of the EVs, the energized composite is nonflammable because it uses aqueous (water-based) electrolytes instead of the conventional flammable organic electrolytes.[8] Moreover, it possesses high cycle life of almost 8500 charge–discharge cycles with more than 90% retention compared to the conventional Li-ion batteries (LIBs), which only show ≈2000 cycles.[9] This is very important considering the fact that the body shell is supposed to last the vehicle's lifetime.

Though the electrochemical storage area of energized composite exhibited a high areal energy density of 0.31 mWh cm^{-2} at a bend strength of 477 MPa and tensile strength of 518 MPa due to its unique patterned electrode disposition, a design optimization study is missing. Such a study enables achieving maximum possible energy storage while retaining the minimum required tensile and bend strength.[4] Our previous study used 20 mm × 20 mm square patch deposition pattern for electrodes (and electrolyte) and epoxy was applied in the remaining area. However, there can be many configurations by varying these pattern sizes. This will change the ratio of the electrochemical area (EcA) versus epoxy area (EpA). Such a variation in EcA versus EpA will lead to different tensile and bend strengths for the energized composite at different energy storage capabilities.

In energized composites, both tensile strength and bend strength are linked to the ratio and distribution of EcA versus EpA. This study modulates the electrode area as shown in **Scheme 1** and Figure S2, Supporting Information. In order to choose an appropriate dimension for design optimization studies, a 160 mm × 160 mm × 2.3 mm volume (based on seven layers thickness) was initially chosen. However, as such a size is difficult to test experimentally on a universal testing machine (UTM), a representative volume element (RVE) of 160 mm × 30 mm × 2.3 mm was used (for both simulation and experimental) instead, which is given in Figure S1, Supporting Information. This is clearly the smallest volume over which measurements can be made to yield a value representative of the whole composite. As the required sample is in the shape of a bar, this could be easily fabricated and experimentally tested on a UTM for tensile and bend tests based on ASTM standards. Thus, in this work, seven configurations with varying patch sizes: 28 × 28, 24 × 24, 20 × 20, 16 × 16, 12 × 12, 8 × 8, and 4 × 4 mm^2 were chosen for design optimization (Figure S2, Supporting Information). Each of these composites has been simulated with four carbon fiber laminates (two anodes and two cathodes) and three glass fiber laminates (two separators and one insulator) layers such that the total thickness is ≈2.3 mm.

To understand the effect of the EcA versus EpA, seven configurational energized composites have been fabricated and tested on a UTM to confirm the simulation results. The electrochemical performances of various electrode sizes have also been measured using cyclic voltammetry (CV), galvanic charge–discharge, and electrochemical impedance spectroscopy (EIS). This helped us to understand the energy storage capacity versus mechanical

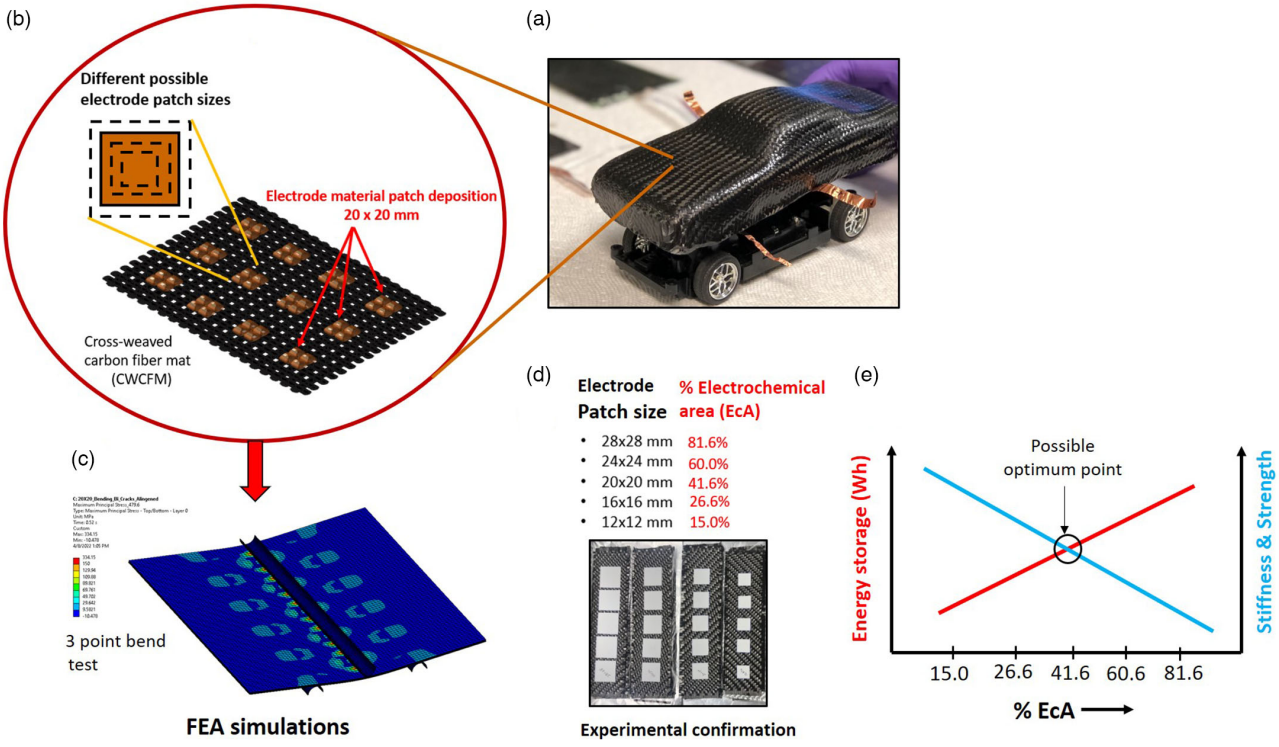

Scheme 1. a) Electric vehicle's body panels that could be replaced with energized composite parts. b) Various square patched electrodes with different EcA versus EpA ratios. EpA is given in black and EcA in brown (square area). c) Representative FEA simulation using ANSYS 2022 R1 for optimizing the stiffness via 3-point bend test. d) Experimental samples for bend and tensile tests with varying EcA versus EpA using representational white patches. e) Energy storage versus %EcA versus stiffness and strength behavior optimization based on specific requirements.

strengths of these energized composites. Finally, the electrochemical and mechanical properties of our energized composite (with optimized design configurations) have been compared against other reported similar energized composites in a Table S3, Supporting Information.

2. Numerical Simulations

2.1. Finite Element Model for the Energized Laminates

Finite element analysis is applied to understand the mechanical behavior of the woven laminates. In this part, seven 3D finite element models (FEMs) with different EcA areas ($160 \times 30 \times 2.3$ mm geometry) are built using ANSYS space claim (ver. 2021 R2 student) on a Windows 10 pro interface. The material properties for carbon fiber/epoxy and glass fiber/epoxy lamina are defined in ANSYS engineering data interface, as given in **Table 1**. The mechanical strength of electrolytes is considered negligible, as also mentioned in our previous study.[4] The epoxy volume percentage decreases as the electrolyte area increases. Hence, continuous degradation of mechanical properties is observed. The elastic modulus of laminas decreases progressively by 1.5% as the patch sizes increase based on the following equation[4,7,10]

$$E_{\mathrm{e-CFRP}} = E_{\mathrm{m}}(1 - (V_{\mathrm{f}} + V_{\mathrm{s}})) + E_{\mathrm{f}} V_{\mathrm{f}} \quad (1)$$

where $V_{\mathrm{f}} + V_{\mathrm{m}} + V_{\mathrm{s}} = 1$; V_{f}, V_{m}, and V_{s} are the volume fractions of fiber, epoxy matrix, and gel electrolyte (supercapacitors), respectively; and E_{f} and E_{m} are the elastic modulus of fiber and matrix, respectively.

The tensile strength of fibers is also progressively reduced with the same fraction as it is directly correlated to the Young's modulus.[10,11] The meshing is performed with ANSYS-workbench mechanical. Node-to-node connectivity is provided to the EcA and EpA elements. Fibers in all layers are assigned the same orientations with the ANSYS ACP-Pre-tool. Laminate damage can be segregated in three ways: fiber damage, matrix damage, and interlaminar delamination.[12] Damage in laminates can be modeled with Hashin's strength criteria, Tsai-Hill, Tsai-Wu, maximum stress, maximum strain, and puck criteria in Ansys.[13] However, the Ansys guide recommends maximum stress, maximum strain, Tsai-Wu, and Tsai-Hill criteria for woven plies.[14] We have used maximum stress criteria to initiate damage in all the laminates owing to their simplicity (Section S1.2, Supporting Information). The damage evolution is characterized by material property degradation[15] and the damage properties are integrated into the laminas material properties in the engineering data. Cohesive zone modeling (CZM) is applied to simulate the effect of electrolyte area in interlaminar layers of the composite (theory discussed in Section S1.3, Supporting Information).[16] Further in this study, glass fiber reinforced polymer is abbreviated as GFRP.

Table 1. Material properties of CFRP and GFRP for single ply.[17,18]

Material property	Carbon fiber/epoxy composite	Glass fiber/epoxy composite[17]
Longitudinal and transverse elastic modulus ($E_{11} = E_{22}$)	36.1 GPa	23.4 GPa
Poisson's ratio (in-plane) (ν_{12})	0.04	0.153
Poisson's ratio (out-o-plane) ($\nu_{13} = \nu_{23}$)	0.30	0.25
In-plane shear modulus (G_{12})	3.30 GPa	3.52 GPa
Out-of- plane shear modulus ($G_{13} = G_{23}$)	2.70 GPa	1.36 GPa
Longitudinal and transverse tensile strength ($X_{\mathrm{t}} = Y_{\mathrm{t}}$)	513 MPa	449 MPa
Longitudinal and transverse compressive strength ($X_{\mathrm{c}} = Y_{\mathrm{c}}$)	437 MPa	336 MPa
In-plane shear strength (S_{12})	120 MPa	45.2 MPa
Out-of-plane shear strengths ($S_{13} = S_{23}$)	55 MPa	37.6 MPa

2.1.1. Tensile Test Model

Tensile and 3-point bending tests are performed for all the above-mentioned configurations (Figure S2, Supporting Information) with ANSYS mechanical, as shown in **Figure 1**. Figure 1a shows the schematic of the tensile FEM for a 20×20 EcA patch laminate. Fixed support is applied to one end of the FEM in the tensile test, as shown in Figure 1a. Additionally, the displacement is applied at the opposite end of the FEM. The FEM for the tensile test has 16 488 nodes and 8939 elements. The "static structural" method is applied with sufficient refined mesh (2 mm).

2.1.2. Flexural Test Model

FEM for the 3-point bend test is developed similar to the 3-point bend test FEM of Bouligand CFRP samples developed by Mencattelli et al.[19] The modeling of the composite is kept the same as the tensile test. However, additional bending fixtures (10 mm diameter) with structural steel properties are incorporated as SHELL 181 elements. Frictionless surface-to-surface contact is maintained between the bending fixtures and the laminate. Fixed support boundary conditions are applied to the bending fixtures in parallel to the z-direction displacement boundary condition to the top pin of the laminate, as shown in Figure 1b. The 3-point bend test FEM has 18 022 nodes and 10 334 elements. Figure 1c illustrates the various element types corresponding to the different geometries involved in the FEM. The laminate is modeled with SOLID 185 elements; however, SHELL 181 elements are used to model bend fixtures. The epoxy region of interlaminar layers is modeled with INTER205 interface elements, as shown in Figure 1d. The electrolyte zones are modeled as open cracks in laminates, as shown in Figure 1e.[20] These open cracks function as stress singularities regions in the laminates due to the negligible mechanical strength of the gel electrolyte. Figure 1f represents the stacking sequence of plies for all laminates. All laminates follow the same stacking sequence of CFRP and GFRP alternate layers.

2.2. Finite Element Analysis: Results and Discussion

2.2.1. Tensile Tests

The load–displacement curves with a maximum displacement of 8 mm are shown in Figure 3a for the tensile FEM.

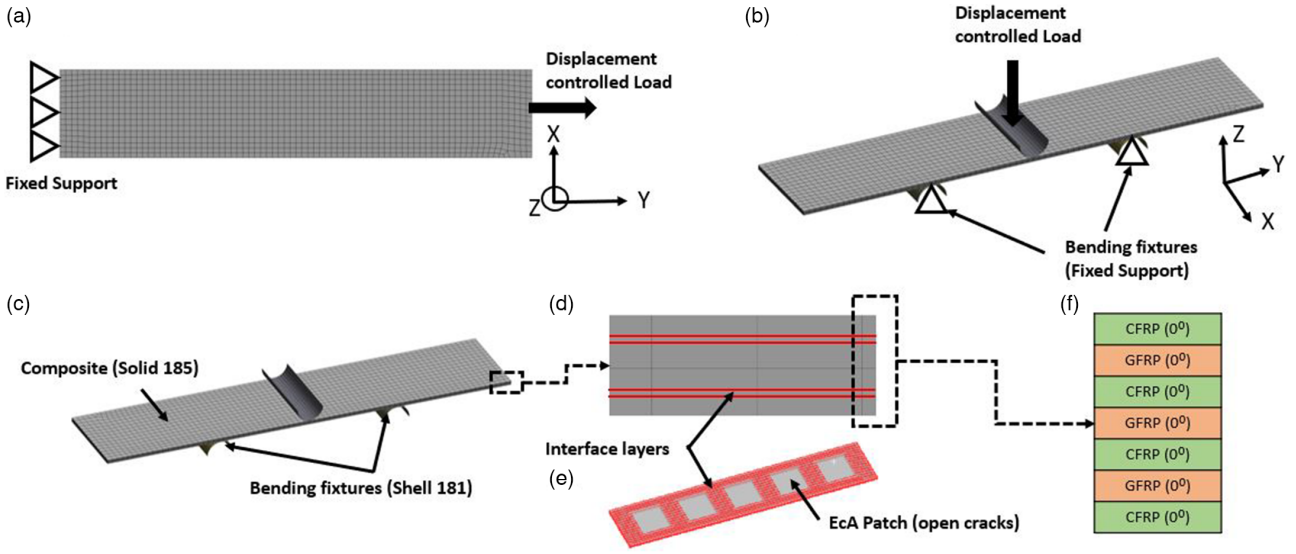

Figure 1. FEM of energized composite: a) schematic of the 3 PB test; b) schematic of the 3 PB test; c) mesh description; d,e) schematic showing interface layers and open cracks in 20 × 20 EcA laminate; f) stacking sequence.

The progressive reduction in the stiffness with the increased EcA area is mainly due to the continuous reduction in the elastic modulus of the composite, as explained earlier.[4]

The simulation is stopped at the first significant reduction in load values, indicating the initiation of damage in the composite material. Jarrah et al.[21] observed similar behavior of the load–displacement curve in the tensile test of composite laminates of CFRP and GRFP. Riccio et al. demonstrated that load–displacement is less sensitive to the mesh size.[22] Therefore, a mesh of 2 mm is considered sufficient for the analysis. The maximum possible load (force in N) values of different configurational designs before damage initiation are shown in **Table 2** (along with their respective %EcA). **Figure 2**a shows the load–displacement curves for various configurations. It is clear from the obtained results that there is a minor variation between various configurations for maximum load-bearing ability in the tensile test. The reason is further explained after experimental studies in Section 3.2. The simulation results given in Table 2 also show the longitudinal stiffness (from the slope of the load–displacement curves) obtained for each of these configurations. Further, the tensile strength has been estimated from the average normal stresses in laminates, which can be seen reducing very mildly for different configurations, as shown in Figure 2b. It has values: 552, 540, 531, 523, 515, 505, and 487 MPa corresponding to 4 × 4, 8 × 8, 12 × 12, 16 × 16, 20 × 20, 24 × 24, and 28 × 28 patch size laminates, respectively. These values have also been tabulated in the last column of Table 2. The progressive reduction in the tensile strength is mainly attributed to the reduction in the volume fraction of the matrix and, ultimately, elastic modulus.[4] The percentage normal strain plots corresponding to respective maximum stress values, as shown in Figure 2c, show that the deformation behavior is similar in all the composites, which illustrates that the effect of EcA is less significant on the tensile failure behavior of composites. Figure 2d shows the zoomed-in view of the % normal strain (γ-direction) for a 20 × 20 EcA composite.

Table 2. Maximum sustained force, stiffness, and ultimate strength for simulated tension test of energized composite samples for different configurations.

Electrolyte patch size (mm × mm)	Tensile Test			
	%EcA	Force, N [F_{max}]	Longitudinal stiffness [N mm^{-1}]	Tensile strength [MPa]
4 × 4	1.67	66 844	8534	552.42
8 × 8	6.67	64 040	8420	540.46
12 × 12	15.00	62 392	8306	531.52
16 × 16	26.67	60 459	8198	523.51
20 × 20	41.67	58 273	8074	515.1
24 × 24	60.00	57 074	7977	505.3
28 × 28	81.60	53 946	7870	487.35

2.2.2. Flexural Tests (3-Point Bend Tests)

Similarly, load–displacement curves obtained for 3-point bend tests of different configurations are shown in **Figure 3**a. However, as can be observed in load–displacement curves (Figure 3a), laminates' stiffness (slope) decreases sharply after deformation reaches a specific value. This is mainly attributed to the first ply failure of composite, also called as "knee effect".[23] The maximum load values at the first failure are shown in **Table 3** for various configurations. Unlike the results of the tensile tests, the bending stiffness calculated from the slope of the load–displacement curve decreases significantly as the amount of electrolyte (EcA) is increased. The bending stiffness, as presented in Table 3, reduces from 656.18 to 160.29 N mm^{-1} as the electrolyte area increases from 1.67% (4 × 4 configuration) to 81.60% (28 × 28 configuration). The force–displacement curves of

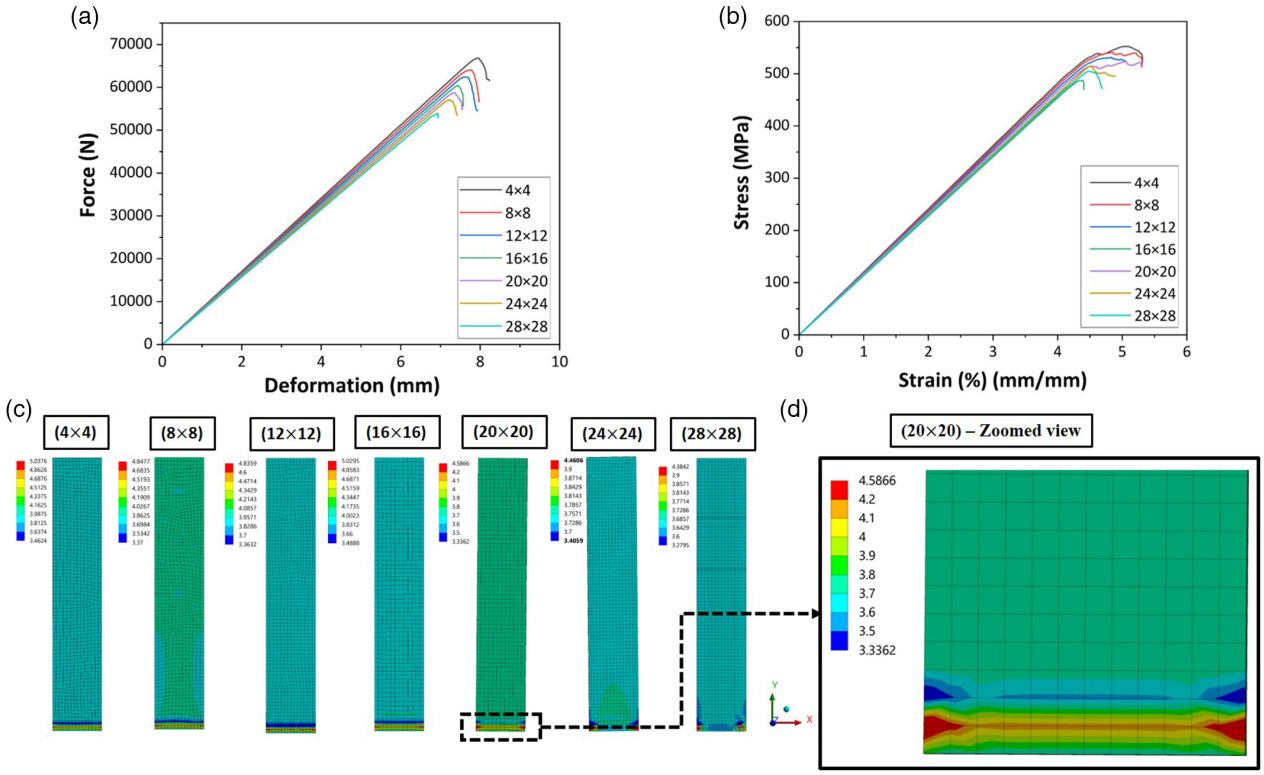

Figure 2. Tensile test FEA results for energized composites with different patch areas: a) force versus deformation plot; b) average stress versus average strain curve; c) % normal strain (γ-direction) for energized composite laminates to their corresponding maximum stress values; d) zoomed-in view of % strain illustrating the behavior of failure in laminates.

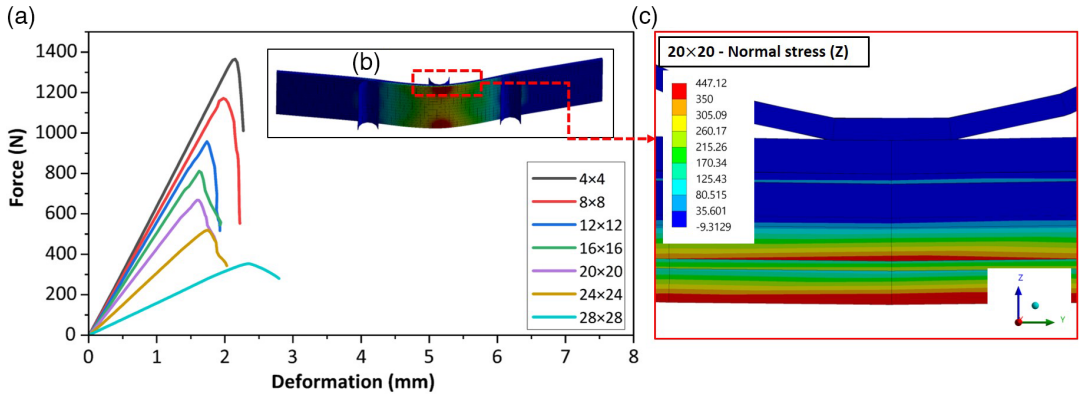

Figure 3. a) 3-point bend test load–displacement curves from FEA for energized composites with different patch areas; inset image (b) shows a full and zoomed-in plot for normal stress for 20 × 20 EcA composite at maximum force; c) zoomed-in view illustrating the higher stresses in the inner layers as a result of incorporating electrolytes in composites.

various laminates clearly follow a particular trend; as EcA increases, the F_{max} value decreases. These results are further discussed in Section 3.2. As an example, normal stress (in *Z*-axis—out of the plane) results are shown for 20 × 20 EcA composite in Figure 3b with a contour plot showing peak value in red, corresponding to the maximum load. This peak value is observed at the bottom layer of the composite, as shown in the zoomed-in plot of Figure 3c. These peak stresses are due to interlaminar shearing because EcA is modeled as open cracks in the FEM. As a result, the mechanical strength of energized composite decreases as the electrolyte area increases.

3. Experimental Studies: Results and Discussion

To confirm the simulation results, both bending and tensile experiment tests were performed. Samples of the energized composite were made and tested for their mechanical strengths

Table 3. Maximum sustained force, bending stiffness, and strength for simulated 3-point bend test of energized composite samples for different configurations.

Electrolyte patch size [mm × mm]	Flexural test			
	%EcA	Force, N [F_{max}]	Bending stiffness [N mm^{-1}]	Bend strength [MPa]
4 × 4	1.67	1365.4	656.18	903.10
8 × 8	6.67	1172.7	606.30	775.80
12 × 12	15.00	957.8	569.48	633.70
16 × 16	26.67	811.15	517.91	536.78
20 × 20	41.67	667.64	436.20	447.20
24 × 24	60.00	519.13	313.70	343.46
28 × 28	81.60	353.87	160.29	234.13

on a UTM in accordance with the relevant industry standards. The flexural test, also known as the 3-point bend test, was performed to determine the bending stiffness and strength based on the recommendations of ASTM D790.[24] A tension test was performed to determine the tensile stiffness and strength of the samples following the guidelines given as per ASTM D3039.[25]

3.1. Mechanical Characterizations

3.1.1. Flexural Test

All seven configurations of energized composite with varying EcA versus EpA ratios were fabricated and tested for their bending stiffness and strength in accordance with the recommendations of ASTM D790.[24] Further details of sample preparation are given in Section S2.1, Supporting Information.

The 3-point bend test was performed to determine flexural (bending) strength and stiffness. Figure S4a, Supporting Information, shows the experimental setup for the 3-point bend test. The test was performed on an Instron 3369 UTM, in accordance with the recommendations of ASTM D790.[24] Each sample was tested under a load cell of 50 kN, with a minimum span length (l) of 70 mm. This satisfies the necessary condition of D790; the span to thickness (L:H) ratio of the samples should be greater than 16:1. The test was performed under a displacement-controlled condition where crosshead speed was set to 3 mm min^{-1}.

After completing 3-point bend tests of these seven composites on the UTM, their load (N) versus deflection (mm) curves are plotted, as shown in **Figure 4**b. For comparison purposes, the load versus deflection curves from simulation studies are shown in Figure 4a. Several of these curves clearly exhibit all three

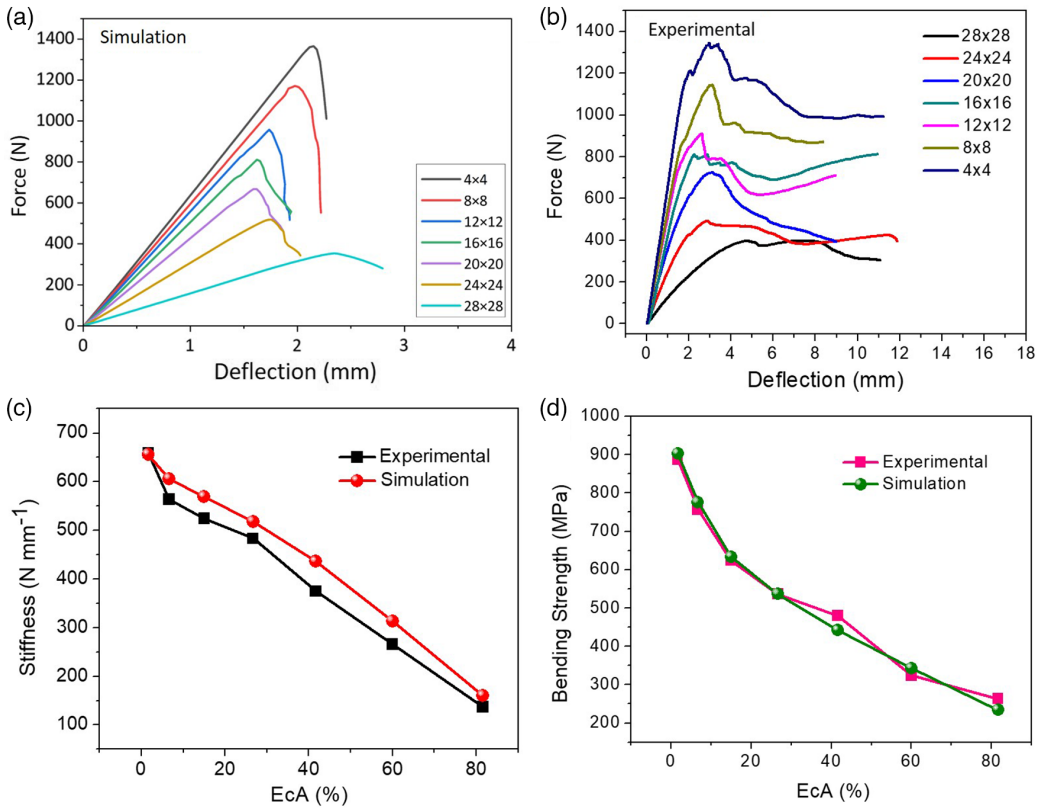

Figure 4. a) Force versus displacement curves of various configurations of the energized composite obtained through simulation studies on 3-point bend tests. b) Force versus displacement curves of various configurations of the energized composite obtained through experimental studies (3-point bend tests). c) Bending stiffness versus EcA (%) curve from simulation and experimental studies. d) Bending strength versus EcA (%) curves obtained for simulation and experimental studies.

characteristics: elastic region, elastic–plastic elongation, and plastic deformation followed by breaking. All of these curves start with linear elastic behavior where force is proportional to the deflection (mm). After reaching a certain deflection value, the proportionality relation no longer exists and the curves tend to bend more toward x-axis but still keep going up. This is where they show elastic–plastic behavior. After reaching a maximum value of force (F_{max}), these curves take a dip and this is where they enter a total plastic deformation zone where the curve starts to come down and continues with increasing deflection till it ends (where the sample breaks).

In composites (Figure 4b), for the purposes of technical and scientific relevance, only the section of the curves where F_{max} is achieved is considered significant. Beyond this region, the sample is assumed to be fractured.[26] After this fracture point, the behavior of the curve is totally random because the breaking starts via internal crack propagation in multiple directions. Based on the data obtained from testing different samples (Figure 4b), the $4 \times 4\,mm^2$ configuration exhibited F_{max} of about 1342 N (highest among all configurations) at a deflection (δ) of 2.96 mm. The reason for it showing the highest F_{max} is its lowest EcA of just 1.96%. Alternatively, $28 \times 28\,mm^2$ configurations with the highest EcA of 81.6% exhibited the lowest F_{max} of just 397.71 N at a deflection of 4.78 mm. All other configurations exhibited their F_{max} between these two extremes: $-8 \times 8\,mm^2$: $F_{max} = 1144$ N, $12 \times 12\,mm^2$: $F_{max} = 943$ N, $16 \times 16\,mm^2$: $F_{max} = 810$ N, $20 \times 20\,mm^2$: $F_{max} = 725$ N, and $24 \times 24\,mm^2$: $F_{max} = 490$ N. The bending strength (MPa) and bending stiffness ($N\,mm^{-1}$) are both determined within the region up to F_{max}. Following bending equations have been used to determine bending strength and stiffness[27,28]

$$\text{Bending stiffness}\,(S) = \frac{F}{\delta} \tag{2}$$

$$\text{Bending equation:}\ \frac{M}{I} = \frac{E_{Comp.}}{R} = \frac{\sigma}{Y} \tag{3}$$

$$\text{Flexural (Bending) strength}\,(\sigma_{fs}) = \frac{3F_{max}l}{2bh^2} \tag{4}$$

where F is the obtained reaction force (in N), δ is the deflection (in mm) of the center point of the composite (obtained from the crosshead movement in UTM), M is the bending moment, I is the moment of inertia of the cross section, E_{comp} is the effective Young's modulus of composite, R is the radius of curvature, l is the span length in the bend test, b is the width of the composite, and h is the thickness of the composite.

First, the bending stiffness (S_b) was determined from the slope (using Equation (2)) of the linear elastic region of these curves, where proportionality between F and δ was maintained (Figure 4b). This was clearly visible in the deflection (δ) range of 0–2 mm for all of the configurations. The $4 \times 4\,mm^2$ configuration exhibited S_b of about $659.29\,N\,mm^{-1}$ (highest among all configurations), while the $28 \times 28\,mm^2$ showed S_b value reaching only $137.06\,N\,mm^{-1}$ as given in Figure 4c. All other configurations have their stiffness values between these two extremes: $8 \times 8\,mm^2$: $S_b = 564.02\,N\,mm^{-1}$, $12 \times 12\,mm^2$: $S_b = 524.82\,N\,mm^{-1}$, $16 \times 16\,mm^2$: $S_b = 483.41\,N\,mm^{-1}$, $20 \times 20\,mm^2$: $S_b = 375.05\,N\,mm^{-1}$, and $24 \times 24\,mm^2$: $S_b = 265.66\,N\,mm^{-1}$. Stiffness results from all of these seven configuration composites are plotted against their respective %EcA in Figure 4c to understand how the ratio of EcA versus EpA governs the overall stiffness of the energized composite. The results of simulation studies have also been plotted in the same perspective in Figure 4c. It can be seen that experimental stiffness results are in tandem with the simulation studies. Experimental stiffness is slightly lower in most cases than the simulation stiffness. The reason could be attributed to the manual hand layup process in the fabrication of these composites, where it is difficult to control the correct ratio of EcA versus EpA while fabricating.

Using F_{max} value for each of the configurational composite and their respective dimensions (b, h), the ultimate value of the flexural strength (σ_{fs}), also known as bending strength, was calculated with the help of Equation (4). Just like stiffness behavior versus %EcA, the $4 \times 4\,mm^2$ configurational composite exhibited the highest bending strength of 887.9 MPa. On the other hand, the $28 \times 28\,mm^2$ configurational composite fractured with a bending strength of only 263.13 MPa. The bending strength of all other configurational composites was calculated and plotted against their respective %EcA, as shown in Figure 4d. For all other configurations, the bending strength ranged between these two extremes and showed an exponential drop as the %EcA was increased. The values were as follows: $8 \times 8\,mm^2$: $\sigma_{fs} = 756.8$ MPa, $12 \times 12\,mm^2$: $\sigma_{fs} = 623.9$ MPa, $16 \times 16\,mm^2$: $\sigma_{fs} = 535.9$ MPa, $20 \times 20\,mm^2$: $\sigma_{fs} = 479.6$ MPa, and $24 \times 24\,mm^2$: $\sigma_{fs} = 324.19$ MPa. The bending strength for the composites was also calculated from F_{max} values obtained for various configurations in the simulation studies. They are given in Table 1 and also plotted against the experimentally obtained values in Figure 4d. The experimental bend strengths for composites are in close proximity to the simulated bend strength with a few minor deviations owing to the manual layup fabrication method of the composites.

3.1.2. Tension Test

All seven configurations of energized composite with varying EcA versus EpA ratios were experimentally fabricated and tested for their tensile strength in accordance with the recommendations of ASTM D3039.[25] Further details of sample preparations are given in Section S2.2, Supporting Information.

All seven configurational composite samples were subjected to a uniaxial tension test on an Instron 3380 UTM, having a rated capacity of 100 kN. Figure S4b, Supporting Information, shows the experimental setup for the uniaxial tension test on the energized composite samples. The test was performed under a displacement-controlled environment where the crosshead speed was kept constant at $2\,mm\,min^{-1}$ based on the recommendations of ASTM D3039.[25]

Load (N) versus displacement (mm) data were generated under displacement-controlled conditions for all seven configurational composites. Engineering stress versus strain data were obtained by using load versus displacement data through dimensional calculations of the samples. The results are plotted in **Figure 5**a,b. Interestingly, unlike the results in the bending tests, uniaxial tension tests tend to generate stress versus strain curves

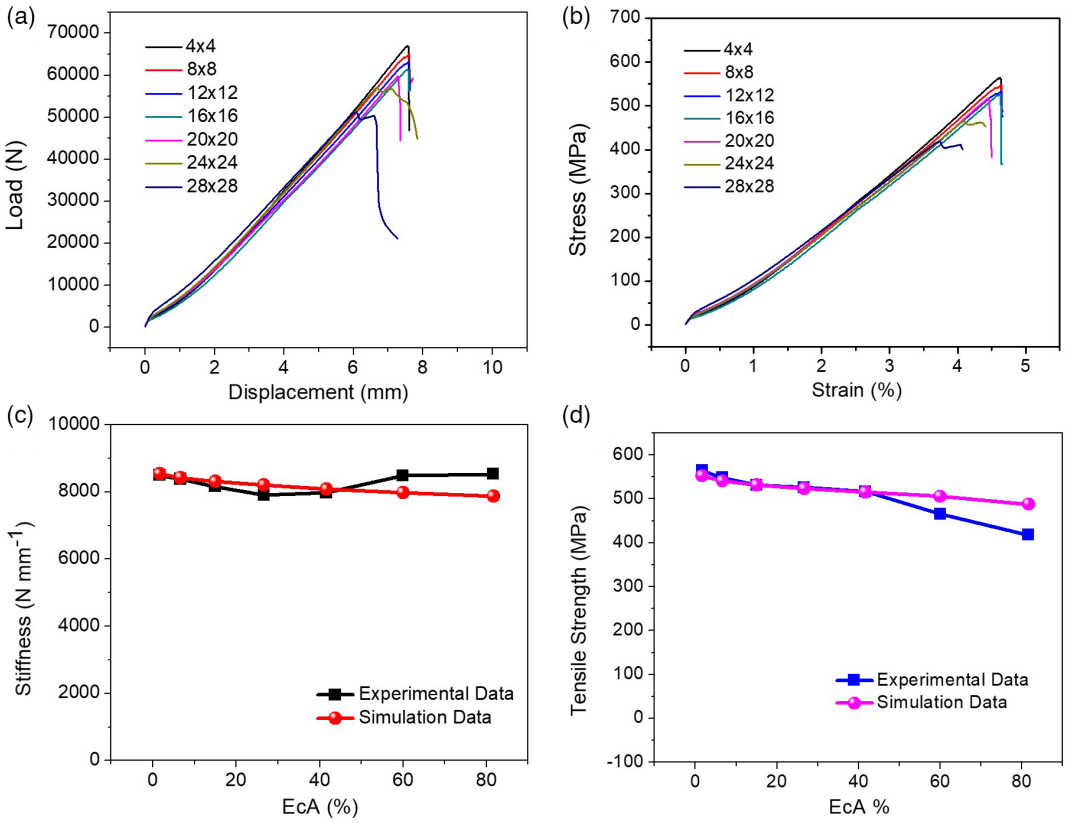

Figure 5. a) Force versus displacement curves of various configurations of the energized composite obtained through experimental studies of tension test. b) Tensile stress versus strain curves of various configurations of the energized composite obtained through experimental studies of tension tests. c) Longitudinal stiffness versus EcA (%) curve obtained for both simulation and experimental studies. d) Tensile strength versus EcA (%) curve obtained for both simulation and experimental studies.

(and load–displacement curves) for all configurations with nearly similar slopes. The slope of the stress versus strain curves of these composites gives the Young's modulus for each of them. The relation of this modulus to the volume fractions of fiber and epoxy can very well explain this result of nearly similar slopes for tension tests of these different configurations.[28] If the volume fraction of the fibers in the composite is given by V_f, and the volume fraction of the epoxy (or matrix) is given by V_m, then the Young's modulus for any regular fiber–epoxy composite can be given by the relation[29]

$$E_{CFRP} = E_m(1 - V_f) + E_f V_f \quad (5)$$

$$\text{however, } V_f + V_m = 1 \quad (6)$$

where E_m is the Young's modulus of the epoxy (matrix) and E_f is the Young's modulus of the fibers. However, in the case of energized composite (e-CFRP), there is a separate volume occupied by the electrode materials and electrolyte (supercapacitor patch areas) where the Young's modulus is negligible compared to epoxy and the fibers. If the volume fraction of supercapacitors is given by V_S, then Young's modulus for energized composite is given by[4,29]

$$E_{e-CFRP} = E_m(1 - (V_f + V_S)) + E_f V_f \quad (7)$$

However, in the case of carbon fiber-based composites, the value of $E_f >> E_m$.[30] Thus, even in the case of different configurations of energized composite (each configuration will have a different V_S), as overall Young's modulus largely depends only on E_f, we do not observe any significant changes in the slope of these curves.

Figure 5c shows the longitudinal stiffness versus %EcA of different configurational composites as obtained from the slope of their respective load versus displacement curves. For comparison purposes, longitudinal stiffness (S_l) values from the simulation study have also been plotted in the same figure and experimental values are similar to the simulation values. For $4 \times 4\ mm^2$ composite, the obtained stiffness value is around $8493\ N\ mm^{-1}$, whereas the $28 \times 28\ mm^2$ composite exhibited a stiffness of $8525\ N\ mm^{-1}$. For all other configurations, the stiffness values ranged as follows: $8 \times 8\ mm^2$: $S_l = 8380\ N\ mm^{-1}$, $12 \times 12\ mm^2$: $S_l = 8160\ N\ mm^{-1}$, $16 \times 16\ mm^2$: $S_l = 7897\ N\ mm^{-1}$, $20 \times 20\ mm^2$: $S_l = 7972\ N\ mm^{-1}$, and $24 \times 24\ mm^2$: $S_l = 8478\ N\ mm^{-1}$. Hence, there is a minor change in the longitudinal stiffness value for all the configurations and the overall value hovers around $8000\ N\ mm^{-1}$.

Figure 5d shows the ultimate tensile strength of energized composite plotted against its respective %EcA. This is obtained from the ultimate stress values of stress versus strain curves (from Figure 5b) of various configurational composites tested.

The majority of configurations showed almost similar tensile strength except for a few outliers like 28×28. The $4 \times 4\ mm^2$ composite showed the highest tensile strength of 563 MPa, while $28 \times 28\ mm^2$ composite showed a still good tensile strength of 417.73 MPa. For all other configurations ultimate strength values were as follows: $8 \times 8\ mm^2$: $\sigma_t = 547.56$ MPa, $12 \times 12\ mm^2$: $\sigma_t = 531.15$ MPa, $16 \times 16\ mm^2$: $\sigma_t = 525.8$ MPa, $20 \times 20\ mm^2$: $\sigma_t = 516.23$ MPa, and $24 \times 24\ mm^2$: $\sigma_t = 465.49$ MPa. For comparison purposes, the ultimate strength values from the simulation study have also been plotted in the same Figure 5d. It can be observed that the results of the experimental study are in close proximity to simulation studies. However, as the percentage of EcA goes beyond 60% (for configurations like 24×24 and $28 \times 28\ mm^2$), it becomes difficult to control the area in which epoxy spreads because this is done manually by Layup method. Thus, it can cause minor deviation from the expected results in stiffness and strength while testing the composites. This is shown by the outlier values in Figure 5c,d.

3.2. Electrochemical Characterizations

To determine the effect of EcA versus EpA ratio on the energy storage ability of energized composite, different patch sizes were assembled in the form of the asymmetric solid-state devices with PAM/Na_2SO_4 gel electrolyte, as discussed in our previous study.[4] The cathode is made up of $VGCF/Mn_3O_4$ electrodes on a carbon fiber mat (as a current collector). In contrast, the anode is made up of $VGCF/MoO_3$ electrode material on a carbon fiber mat (as a current collector). These devices (4×4, 8×8, 12×12, 16×16, 20×20, 24×24, and $28 \times 28\ mm^2$) were assembled using a similar approach as that of energized composite. After curing, the samples were tested on a CHI Impedance analyzer for their electrochemical characteristics.

First, CV study was performed on these devices with varying patch areas at a scan rate of 5 mV s^{-1}. **Figure 6**a shows the various cyclic voltammograms obtained for different patch sizes. The area enclosed by a cyclic voltammogram determines its capacitance, i.e., charge storage ability.[31] The larger the area, the higher is the charge storage ability. This is also evident from Figure 6a. A patch area of $4 \times 4\ mm^2$ (black) exhibited the smallest area enclosed in a CV curve, while the patch area of $28 \times 28\ mm^2$ (navy blue) showed the highest enclosed loop area. Based on the area enclosed by these cyclic voltammograms, the capacitance for each of these patch sizes was also determined: $4 \times 4\ mm^2$: 88 mF, $8 \times 8\ mm^2$: 352 mF, $12 \times 12\ mm^2$: 792 mF, $16 \times 16\ mm^2$: 1408 mF, $20 \times 20\ mm^2$: 2200 mF, $24 \times 24\ mm^2$: 3168 mF, and $28 \times 28\ mm^2$: 4312 mF. Based on this data, it is evident that the largest area devices have the highest charge storage ability.

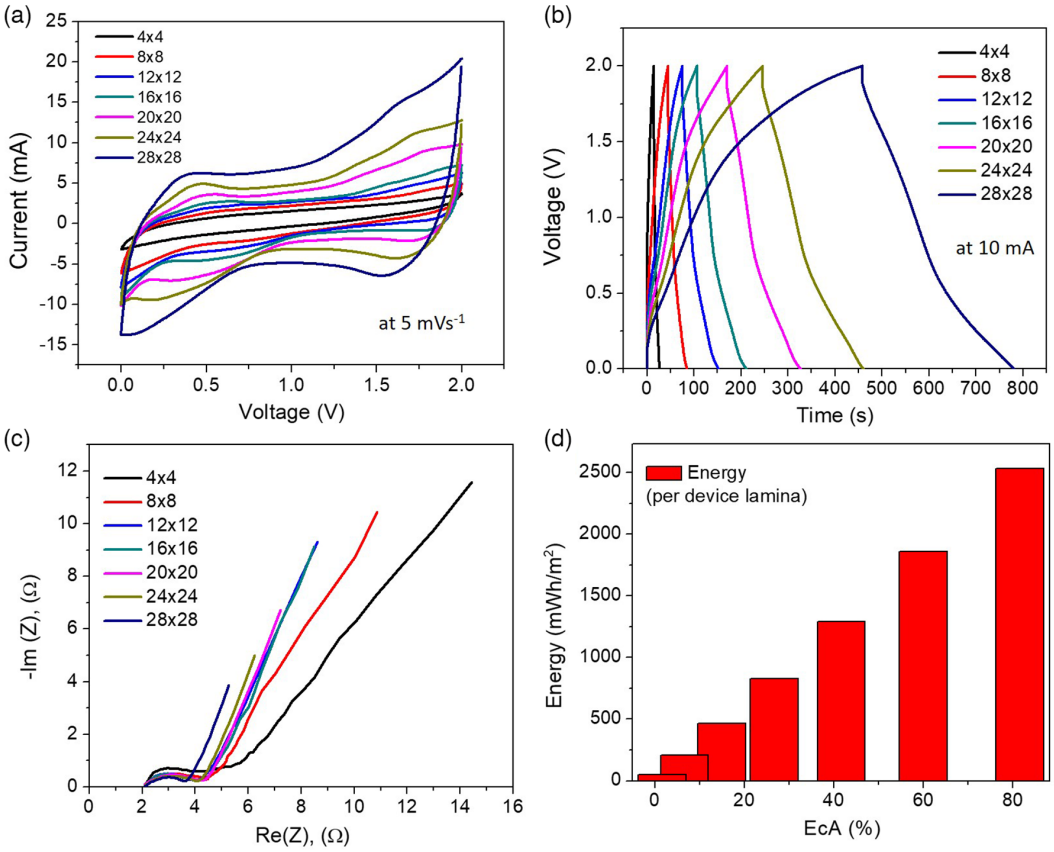

Figure 6. a) Cyclic voltammograms of various patch sizes of the fabricated energized composite obtained at a scan rate of 5 mV s^{-1}. b) Galvanic charge–discharge plots of various patch sizes obtained at a charge–discharge current of 10 mA. c) EIS of various patch sizes. d) Energy storage ability per device lamina of various configurations of energized composite based on their %EcA.

Next, these devices were subjected to a galvanic charge–discharge test at a current of 10 mA. GCD plots for these different patch sizes are shown in Figure 6b. Again, a similar pattern was obtained where the highest area electrode $28 \times 28\ mm^2$ delivered the highest discharge time of 323 s, whereas the lowest area electrode $4 \times 4\ mm^2$ delivered a discharge time of just 12 s at 10 mA charge–discharge current. The other patch area electrode had their discharge time between these two extremes: $8 \times 8\ mm^2$: 41 s, $12 \times 12\ mm^2$: 75 s, $16 \times 16\ mm^2$: 104 s, $20 \times 20\ mm^2$: 155 s, and $24 \times 24\ mm^2$: 216 s.

Further, to determine the impedance of these patch sizes, the fabricated devices were subjected to electrode impedance spectroscopy (EIS). The obtained EIS spectra for these patch sizes are plotted in Figure 6c in the form of a Nyquist plot. Equivalent series resistance (ESR) for various patch sizes was obtained from the abscissa of the curves in the initial high-frequency region.[32] Almost all of these curves intersect the real axis of the spectra at a value of $\approx 2.08\ \Omega$. This can be explained because the electrode material and the electrolyte are exactly the same in all of the patches; hence, the ESR value should be the same for all devices.[33] Next, the charge transfer resistance (R_{ct}), also known as faradaic resistance, is obtained from the cut (chord) on the real axis by the imaginary semicircle arc made by these plots in the high-frequency region.[33] Unlike the constant ESR, the charge transfer resistance is inversely dependent on the patch area of the electrodes. The smallest $4 \times 4\ mm^2$ patch exhibited the highest R_{ct} of $\approx 3\ \Omega$, while the largest $28 \times 28\ mm^2$ patch size showed the least R_{ct} of $\approx 1.5\ \Omega$. This can be explained by the fact that a larger patch size means a larger area of the current collector (carbon fabric) that can better facilitate charge transfer, hence showing a lower resistance. A similar trend was shown in the low-frequency regions of Nyquist plots, where the slope of the plots determines the leakage resistance (R_L). Clearly, the 4×4 patch size (smallest area) had the smallest slope showing high leakage resistance, while 28×28 patch size (largest area) had a higher slope signifying low leakage resistance. All other patch area devices offered leakage resistance in between these two extremes.

Based on the charge storage value and EcA versus EpA ratio, various configurations of the energized composites are categorized based on their energy storage ability (per device laminate). A bar chart showing this energy storage ability based on EcA is given in Figure 6d. The 4×4 patch size configuration has the lowest EcA versus EpA ratio (i.e., lowest %EcA). However, it exhibits the highest tensile and bend strength (as discussed previously) but offers the energy storage ability of $51.67\ mWh\ m^{-2}$ only. On the other hand, the highest patch size device of 28×28 offered a high energy storage value of $2531\ mWh\ m^{-2}$. All other configurations showed energy storage ability directly proportional to their patch sizes (i.e., %EcA): $8 \times 8\ mm^2$: $206.66\ mWh\ m^{-2}$, $12 \times 12\ mm^2$: $464.99\ mWh\ m^{-2}$, $16 \times 16\ mm^2$: $827.96\ mWh\ m^{-2}$, $20 \times 20\ mm^2$: $1291\ mWh\ m^{-2}$, and $24 \times 24\ mm^2$: $1859\ mWh\ m^{-2}$.

4. Conclusion

In this work, we have performed a design optimization study on the tensile strength, bending strength, and electrochemical energy storage ability of our multifunctional energized composite. We have designed different configurations of energized composites by modulating the ratios of EcA versus EpA. Further, these configurations have been simulated using ANSYS software to check their tensile strength and bend strength by uniaxial tension test and a 3-point bend test. To confirm the results of simulation studies, the exact replica of these composites has been fabricated in the lab and was also tested on an Instron UTM machine, based on the relevant ASTM standards for tensile and bend test. Further, to assess the energy storage ability of the configuration based on their patch size, electrochemical characterizations like CV, galvanic charge–discharge tests, and EIS have been performed. It can be concluded from the results that as the EcA on the laminates of energized composite is increased (i.e., the EpA is reduced), there is an exponential drop in the bending strength of the composite, while the tensile strength almost remains constant. An increase in the EcA also correlates to the higher energy storage ability in energized composites. By analyzing the bending, tensile, and electrochemical test results for various design configurations of energized composite, a specific configuration for each body panel in the EV can be chosen for desired maximum charge storage while maintaining minimum tensile and bending strengths. Results from this study could help in the faster adoption of energized composite technology in the EV industry, which will also help to extend the range of EVs making them more popular among the customers

Supporting Information

Supporting Information is available from the Wiley Online Library or from the author.

Acknowledgements

J.T. acknowledges National Science Foundation (IIP-2122779) for the financial support. Raman spectrum was taken using an instrument supported by NSF MRI grant no. 1920050. J.T. also acknowledges Nissan Technical Center, North America (MI), USA for the partial support of the work.

Conflict of Interest

The authors declare no conflict of interest.

Data Availability Statement

Research data are not shared.

Keywords

dual-function composites, energized carbon fiber reinforced polymer (e-CFRP), electric vehicle (EV) energy storage, EV structural batteries, mechanical properties, supercapacitors

Received: July 6, 2022
Revised: October 11, 2022
Published online:

[1] S. Potrč, L. Čuček, M. Martin, Z. Kravanja, *Renewable Sustainable Energy Rev.* **2021**, *146*, 111186.
[2] a) P. Geng, L. Wang, M. Du, Y. Bai, W. Li, Y. Liu, S. Chen, P. Braunstein, Q. Xu, H. Pang, *Adv. Mater.* **2022**, *34*, 2107836; b) C. Liu, Y. Bai, W. Li, F. Yang, G. Zhang, H. Pang, *Angew. Chem.* **2022**, *134*, e202116282; c) S. Zheng, Q. Li, H. Xue, H. Pang, Q. Xu, *Natl. Sci. Rev.* **2020**, *7*, 305.
[3] J. A. Sanguesa, V. Torres-Sanz, P. Garrido, F. J. Martinez, J. M. Marquez-Barja, *Smart Cities* **2021**, *4*, 372.
[4] D. Pandey, K. Sambath Kumar, L. N. Henderson, G. Suarez, P. Vega, H. R. Salvador, L. Roberson, J. Thomas, *Small* **2022**, *18*, 2107053.
[5] J. Cherusseri, K. Sambath Kumar, D. Pandey, E. Barrios, J. Thomas, *Small* **2019**, *15*, 1902606.
[6] J. Chang, M. Jin, F. Yao, T. H. Kim, V. T. Le, H. Yue, F. Gunes, B. Li, A. Ghosh, S. Xie, *Adv. Funct. Mater.* **2013**, *23*, 5074.
[7] J. Cherusseri, S. Pramanik, L. Sowntharya, D. Pandey, K. K. Kar, S. Sharma, *Composite Materials*, Springer, Berlin, Heidelberg **2017**, pp. 37–77.
[8] M. Sajjad, M. I. Khan, F. Cheng, W. Lu, *J. Energy Storage* **2021**, *40*, 102729.
[9] X. Han, L. Lu, Y. Zheng, X. Feng, Z. Li, J. Li, M. Ouyang, *ETransportation* **2019**, *1*, 100005.
[10] W. D. Callister, D. G. Rethwisch, *Materials Science and Engineering: An Introduction*, Vol. *9*, Wiley, New York, NY **2018**.
[11] T. Tagawa, T. Miyata, *Mater. Sci. Eng., A* **1997**, *238*, 336.
[12] J.-F. Chen, E. V. Morozov, K. Shankar, *Composites, Part A* **2014**, *61*, 185.
[13] a) R. Hill, The Mathematical Theory of Plasticity, London **1950**; b) S. W. Tsai, *Fundamental Aspects of Fiber Reinforced Plastic Composites*, Wiley-Interscience, New York **1968**; c) C. Sun, A. Kelly, C. Zweben, *Comprehensive Composite Materials*, Vol. *1* **2000**, 641–666.
[14] Ansys *Composite PrepPost User's Guide*, Release 15.0 (Ed: I. ANSYS) **2013**.
[15] S. Lurie, M. Minhat, *Structural Integrity and Durability of Advanced Composites*, Woodhead Publishing, Cambridge, UK **2015**, p. 143.
[16] G. Alfano, M. Crisfield, *Int. J. Numer. Methods Eng.* **2001**, *50*, 1701.
[17] T. Wiczenbach, T. Ferenc, *Arch. Civ. Eng.* **2021**, *67*, 525.
[18] a) A. Inc., *ANSYS*, ANSYS, Canonsburg, PA **2021**; b) B. Yang, Y. Chen, J. Lee, K. Fu, Y. Li, *Thin-Walled Struct.* **2021**, *158*, 107186.
[19] L. Mencattelli, S. T. Pinho, *Composites, Part A* **2020**, *129*, 105655.
[20] a) M. K. Thompson, J. M. Thompson, *ANSYS Mechanical APDL for Finite Element Analysis*, Butterworth-Heinemann **2017**; b) E. Lindgaard, B. Bak, J. Glud, J. Sjølund, E. Christensen, *Eng. Fract. Mech.* **2017**, *180*, 229.
[21] M. Jarrah, E. P. Najafabadi, M. H. Khaneghahi, A. V. Oskouei, *Constr. Build. Mater.* **2018**, *190*, 38.
[22] A. Riccio, C. Palumbo, V. Acanfora, A. Sellitto, A. Russo, *J. Compos. Sci.* **2021**, *5*, 310.
[23] C. Wen, S. Yazdani, *Compos. Struct.* **2008**, *82*, 127.
[24] a) F. Rezaei, R. Yunus, N. Ibrahim, E. S. Mahdi, *Polym.-Plast. Technol. Eng.* **2008**, *47*, 351; b) I. ASTM, *ASTM D790-07*, ASTM International **2007**.
[25] a) J. M. F. D. Paiva, S. Mayer, M. C. Rezende, *Mater. Res.* **2006**, *9*, 83; b) A. ASTM_International, ASTM International, West Conshohocken, PA **2000**.
[26] a) D. D. Chung, D. Chung, *Carbon Fiber Composites*, Butterworth-Heinemann, Newton, Massachusetts, USA **2012**; b) E. C. Botelho, M. C. Rezende, B. Lauke, *Compos. Sci. Technol.* **2003**, *63*, 1843.
[27] a) M. R. Abusrea, S.-W. Han, K. Arakawa, N.-S. Choi, *Composites, Part B* **2019**, *156*, 8; b) W. D. Callister Jr, D. G. Rethwisch, *Fundamentals of Materials Science and Engineering: An Integrated Approach*, John Wiley & Sons, Danvers, Massachusetts USA **2020**.
[28] W. D. Callister Jr, D. G. Rethwisch, *Callister's Materials Science and Engineering*, John Wiley & Sons, Danvers, Massachusetts USA **2020**.
[29] H. Zhu, T. Fan, D. Zhang, *Sci. Rep.* **2015**, *5*, 1.
[30] a) H. Rahmani, S. H. M. Najaf, A. Ashori, M. Golriz, *Polym. Polym. Compos.* **2015**, *23*, 475; b) K. Yang, Y. Yue, W. Zhao, Y. Liang, L. Mei, J. Xue, presented at *IOP Conference Series: Materials Science and Engineering*, Vol. *770*, 8th Global Conference on Materials Science and Engineering (CMSE2019), Sanya, China, 12–15 November **2019**.
[31] Y. Shao, M. F. El-Kady, J. Sun, Y. Li, Q. Zhang, M. Zhu, H. Wang, B. Dunn, R. B. Kaner, *Chem. Rev.* **2018**, *118*, 9233.
[32] a) G. G. G. Costa, R. C. Pietronero, T. Catunda, *Phys. Educ.* **2012**, *47*, 439; b) V. Khomenko, E. Raymundo-Pinero, E. Frackowiak, F. Beguin, *Appl. Phys. A* **2006**, *82*, 567.
[33] A. Noori, M. F. El-Kady, M. S. Rahmanifar, R. B. Kaner, M. F. Mousavi, *Chem. Soc. Rev.* **2019**, *48*, 1272.